Nondispersive wave packets in planar helium

Alejandro González-Melan [*]
Physics Department, Universidad del Valle, Cali, Colombia

Javier Madroñero [†]
Physics Department, Universidad del Valle, Cali, Colombia
and Centre for Bioinformatics and Photonics, Universidad del Valle, Cali, Colombia

(Received 10 July 2019; published 10 January 2020)

Two-electron wave packets found in driven planar helium follow a classical periodic orbit without spreading and are localized in nonlinear resonance islands of the classical phase space. The general mechanism that produces these nondispersive wave packets is the near-resonant coupling between highly correlated, asymmetric, and doubly excited states of the atom with an external periodic electromagnetic field. We provide a full characterization of these two-electron nondispersive wave packets found in the Floquet spectrum of driven planar helium. This includes the characteristic energy spectrum, relatively long lifetimes, and the identification of the resonance states of helium that are responsible for their formation. This is achieved with the help of an efficient quantum treatment of driven planar helium which combines Floquet theory, complex rotation, and the representation of the Hamiltonian in a set of four coupled harmonic oscillators.

DOI: 10.1103/PhysRevA.101.013414

I. INTRODUCTION

The correlated electron dynamics plays an important role in nonequilibrium processes in atomic [1,2], molecular [3–5], and solid-state physics [6–8]. Controlling the electronic dynamics in such systems is therefore essential for further developments. This is, however, not an easy task since the dynamical processes in the atomic and molecular world occur very fast. Nevertheless, important advances in this direction have been achieved: chemical reactions [9–11] and the ionization process [12] of small molecules are controlled by pulses. The motion of the two electrons in the helium atom has been imaged and investigated with the help of attosecond pulses [13,14] and Fano interferences have been built up [15,16]. There have also been advances in the engineering of atomic Rydberg states [17].

Further progress requires a better understanding of the electronic dynamics in few-electron atoms interacting with electromagnetic fields. In this regard, the interaction of light with the helium atom is of special interest, because, despite being the simplest example for a multielectron atom, its dynamics is nonintegrable even from the classical point of view [18]. The helium atom is a realization of the three-body problem with gravitational forces replaced by attractive and repulsive Coulomb interactions. The classical dynamics of helium is in general irregular and chaotic with only small regions of regular motion in phase space [19], which implies the destruction of good quantum numbers in the quantum description [20] and a chaotic structure of the spectrum. The loss of integrability, due to the electron-electron interaction, prevented the application of Bohr's quantization postulates to the helium atom in the early days of quantum mechanics [18,21,22]. Only with the development of modern semiclassical methods in the second half of the 20th century [23,24] and the subsequent semiclassical quantization of helium [25–27], the relation between the nonintegrability of the quantum system and the classical mixed regular-chaotic dynamics was established [20]. Up to date, various theoretical investigations have improved our understanding of two-electron atoms ranging from semiclassical (see [20] for a review) to quantum mechanics including relativistic corrections [28–32].

Since the seminal experiment by Madden and Codling in 1963 [33], where doubly excited states of two-electron atoms have been identified as highly correlated states that cannot be in general described by a simple model based on independent-particle quantum numbers, doubly and highly excited states of helium have attracted the interest of theoreticians and experimentalists. Particularly, the energy regime near the total fragmentation threshold represents a paradigm for electronic correlations in atomic physics. In this regime—which is indeed the semiclassical one in two-electron atoms—the underlying classical chaotic dynamics should influence the quantum spectrum of highly doubly excited states, manifested as semiclassical scaling laws for the fluctuations of excitation cross sections [34–36] or signatures of quantum chaos such as Ericson fluctuations [37,38].

Strong electronic correlations are found in highly asymmetrically doubly excited states of helium which are associated with the highly correlated classical frozen planet configuration (FPC) [39,40]. Theoretical studies for one-dimensional (1D) [41,42] and planar helium [43,44] suggest that under near-resonantly periodic driving these states transform into two-electron nondispersive wave packets (NDWPs) [45].

[*]alejandro.gonzalez.melan@correounivalle.edu.co
[†]javier.madronero@correounivalle.edu.co

However, until now, there has been no definitive evidence of the existence of these objects.

In this paper, we investigate the dynamics of driven doubly excited states of planar helium and the formation of nondispersive wave packets. While the restriction of the system dynamics to a plane is certainly an important approximation that significantly reduces the complexity compared to the full three-dimensional (3D) treatment, it is known that a planar model also provides a good qualitative and quantitative description of the helium atom that improves as the excitation energy approaches the double ionization threshold [35,36,46,47].

Here, we present an efficient numerical treatment of driven helium which allows us to characterize NDWPs in planar helium. In our approach to solve the time-dependent Schrödinger equation (TDSE) describing the dynamics of a two-electron atom interacting with a periodic electromagnetic field, we use a spectral method combined with Floquet theory [48,49]. The method is based on the solution of the TDSE in a basis set composed of eigenstates of the unperturbed Hamiltonian. The diagonalization of the planar atomic Hamiltonian is achieved within the *ab initio* method described in [43,44] which gives an accurate description of the system combining complex dilation and the representation of the Hamiltonian in suitably chosen coordinates without adjustable parameters. Apart from the significant reduction of the size of the matrices involved in the computations, this method allows us to identify the atomic states with the principal contribution to the formation of the NDWP.

This paper is organized as follows. In Sec. II, we present the theoretical description of the unperturbed and driven planar helium. Section III describes the numerical treatment for the solution of the time-dependent Schrödinger equation in the atomic basis. In Sec. IV we present a general description of the classical frozen planet configuration and frozen planet states (FPSs). Section V contains a brief description of the spectral and localization properties of FPSs of planar helium. In Sec. VI we review the classical dynamics of the driven frozen planet configuration. In Sec. VII we present the characterization of nondispersive wave packets in planar helium. Finally, Sec. VIII contains the summary and conclusions.

II. THEORY

A. Hamiltonian

In the center-of-mass system within the infinite nucleus mass approximation, the dynamics of a two-electron atom is governed by the following Hamiltonian, given in atomic units (a.u.) and neglecting relativistic effects:

$$H_0 = \frac{\boldsymbol{p}_1^2}{2} + \frac{\boldsymbol{p}_2^2}{2} - \frac{Z}{r_1} - \frac{Z}{r_2} + \frac{\gamma}{r_{12}}, \tag{1}$$

where the parameter γ characterizes the electron-electron interaction and Z represent the nucleus charge (for helium $\gamma = 1$ and $Z = 2$). The positions of the electrons with respect to the nucleus are denoted by $\boldsymbol{r}_1$ and $\boldsymbol{r}_2$, and $\boldsymbol{p}_1$ and $\boldsymbol{p}_2$ are the respective conjugate momenta.

Hamiltonian (1) is spin independent. Thus, the two-electron wave function $\Phi(q_1, q_2)$ can be written as $\Phi = \Psi(\boldsymbol{r}_1, \boldsymbol{r}_2)\chi(1, 2)$, where $\Psi(\boldsymbol{r}_1, \boldsymbol{r}_2)$ and $\chi(1, 2)$ correspond to the spatial and spin-wave functions, respectively. The Pauli exclusion principle states that the wave function $\Phi(q_1, q_2)$ must be antisymmetric under the electron-electron exchange. Hence, the total wave function is either the product of a symmetric spatial wave function by an antisymmetric spin-wave function, that is a singlet state, or the product of an antisymmetric spatial wave function by a symmetric spin-wave function which corresponds to a triplet state [50].

B. Complex rotation

The energy spectrum of the unperturbed helium atom is organized in series converging to single ionization thresholds, labeled by the principal quantum number N of the inner electron. The series of the single ionization thresholds converges in turn to the double ionization threshold at zero energy. Above the first ionization threshold ($N > 1$), doubly excited states in helium are coupled to the continuum states of the lower-lying series and correspond to resonance states with a finite lifetime. To extract the energies and decay rates of the resonance states presented in the helium spectra, we use the method of complex coordinate rotation [51–55], which was shown to be applicable for the Coulomb potential in Ref. [56].

The complex rotation by an angle θ is generated by the nonunitary operator

$$R(\theta) = \exp\left(-\theta \frac{\boldsymbol{r}\cdot\boldsymbol{p} + \boldsymbol{p}\cdot\boldsymbol{r}}{2}\right), \tag{2}$$

which yields the transformation of the coordinates and momenta according to $\boldsymbol{r} \to \boldsymbol{r}e^{i\theta}$ and $\boldsymbol{p} \to \boldsymbol{p}e^{-i\theta}$, with $\boldsymbol{r} = (\boldsymbol{r}_1, \boldsymbol{r}_2)$ and $\boldsymbol{p} = (\boldsymbol{p}_1, \boldsymbol{p}_2)$.

The rotated Hamiltonian $H(\theta) = R(\theta)HR(-\theta)$ is no longer Hermitian. Nevertheless, its spectrum is related to the spectrum of the original Hamiltonian [51,52,55].

(i) The bound states of H remain unchanged under the transformation.

(ii) The continuum states are rotated downwards by an angle 2θ with the real axis, around its individual threshold.

(iii) Once the rotation angle θ is sufficiently large, the resonance states are exposed and are associated to complex eigenvalues $E_{i,\theta} = E_i - i\Gamma_i/2$, where the real part corresponds to the energy E_i of the resonance, and the imaginary part contains the decay rate Γ_i, which is the inverse of the resonance lifetime.

The eigenvectors $|\Psi_{i,\theta}\rangle$ of the rotated Hamiltonian $H(\theta)$ are normalized for the scalar product

$$\langle\overline{\Psi_{i,\theta}}|\Psi_{j,\theta}\rangle = \delta_{ij} \tag{3}$$

and satisfy the closure relation

$$\sum_i |\Psi_{i,\theta}\rangle\langle\overline{\Psi_{i,\theta}}| = 1, \tag{4}$$

where $\langle\overline{\Psi_{i,\theta}}|$ is the transpose of $\langle\Psi_{i,\theta}|$.

C. Planar treatment of the two-electron atom

In this simplified model, the dynamics of the atom is confined to a plane. A comprehensive description of the representation we use for this model can be found in Refs. [43,44,57].

1. Regularization of the two-dimensional helium Hamiltonian

The regularization of the Coulomb singularities in the Hamiltonian (1) is achieved by transforming the Cartesian coordinates of the electrons (x_1, y_1) and (x_2, y_2) to a set of parabolic coordinates, obtained after three coordinate transformations: a parabolic transformation

$$\mu_i = \sqrt{r_i + x_i}, \quad \nu_i = \sqrt{r_i - x_i}, \tag{5}$$

followed by a rotation by $\pi/4$,

$$\mu_\pm = \frac{\mu_1 \pm \mu_2}{\sqrt{2}}, \quad \nu_\pm = \frac{\nu_1 \pm \nu_2}{\sqrt{2}}, \tag{6}$$

and a second parabolic transformation,

$$x_\pm = \sqrt{r_\pm + \mu_\pm}, \quad y_\pm = \sqrt{r_\pm - \mu_\pm}, \tag{7}$$

where $r_i = \sqrt{x_i^2 + y_i^2}$ $(i = 1, 2)$ and $r_\pm = \sqrt{\mu_\pm^2 + \nu_\pm^2}$. After these transformations, the expressions for the distances r_1, r_2, and r_{12} become polynomial functions in the new coordinates

$$\begin{aligned} 16r_1 &= [(x_+ - y_-)^2 + (x_- + y_+)^2] \\ &\quad \times [(x_+ + y_-)^2 + (x_- - y_+)^2], \\ 16r_2 &= [(x_+ - x_-)^2 + (y_+ + y_-)^2] \\ &\quad \times [(x_+ + x_-)^2 + (y_+ - y_-)^2], \\ 4r_{12} &= (x_+^2 - y_+^2)(x_-^2 + y_-^2). \end{aligned} \tag{8}$$

The time-independent Schrödinger equation $H_0|\psi\rangle = E|\psi\rangle$ is regularized by multiplication with the *Jacobian* of the transformation:

$$J = 16 r_1 r_2 r_{12}. \tag{9}$$

In this way, we obtain the generalized eigenvalue problem (GEVP):

$$\left(-\tfrac{1}{2}T + V\right)|\psi\rangle = EJ|\psi\rangle, \tag{10}$$

where

$$T = 16 r_1 r_2 r_{12}\left(\nabla_1^2 + \nabla_2^2\right), \tag{11}$$

$$V = -32 r_2 r_{12} - 32 r_1 r_{12} + 16 r_1 r_2. \tag{12}$$

It can be shown that the operators involved in this GEVP are polynomial functions of the parabolic coordinates and their partial derivatives [43]. This fact allows us to introduce a set of creation and annihilation operators defined by

$$\begin{aligned} a_{x_\pm} &= \frac{x_\pm + i p_{x_\pm}}{\sqrt{2}}, \quad a_{x_\pm}^\dagger = \frac{x_\pm - i p_{x_\pm}}{\sqrt{2}}, \\ a_{y_\pm} &= \frac{y_\pm + i p_{y_\pm}}{\sqrt{2}}, \quad a_{y_\pm}^\dagger = \frac{y_\pm - i p_{y_\pm}}{\sqrt{2}}. \end{aligned}$$

Then, we define the circular operators in the planes (x_+, y_+) and (x_-, y_-) as

$$\begin{aligned} a_1 &= \frac{a_{x_+} - i a_{y_+}}{\sqrt{2}}, \quad a_2 = \frac{a_{x_+} + i a_{y_+}}{\sqrt{2}}, \\ a_3 &= \frac{a_{x_-} - i a_{y_-}}{\sqrt{2}}, \quad a_4 = \frac{a_{x_-} + i a_{y_-}}{\sqrt{2}}, \end{aligned} \tag{13}$$

which satisfy the usual commutation relations

$$[a_i, a_j] = 0, \quad [a_i^\dagger, a_j^\dagger] = 0, \quad [a_i, a_j^\dagger] = \delta_{i,j},$$

with $i, j = 1, 2, 3, 4$. In this way, we obtain a basis set of tensorial products of harmonic oscillator Fock states:

$$|n_1 n_2 n_3 n_4\rangle = |n_1\rangle \otimes |n_2\rangle \otimes |n_3\rangle \otimes |n_4\rangle, \tag{14}$$

where $n_i = a_i^\dagger a_i$. The appropriate symmetrization of this basis will be discussed in Sec. II C 3.

The major advantage of this representation is that the expressions for J, T, and V are polynomial functions of finite degree of the circular operators a_i and $a_i^\dagger$. In this way, the matrix elements of the GEVP (10) can be calculated analytically [43], and are expressed in normally ordered (creation operators on the left [58]) monomial terms of the form $M = a_1^{\dagger\alpha_1} a_2^{\dagger\alpha_2} a_3^{\dagger\alpha_3} a_4^{\dagger\alpha_4} a_1^{\beta_1} a_2^{\beta_2} a_3^{\beta_3} a_4^{\beta_4}$, where α_i and β_i are integer numbers. Since the number of monomials in the GEVP is finite, the number of coupled basis states is also finite. This determines a set of *selection rules* $\{\Delta n_1, \Delta n_2, \Delta n_3, \Delta n_4\}$, with $\Delta n_i = n_i - n_i'$, if $\langle n_1 n_2 n_3 n_4 | M | n_1' n_2' n_3' n_4' \rangle \neq 0$. For the GEVP (10) all the selection rules satisfy $-4 \leqslant \Delta n_i \leqslant 4$ and $\Delta n_1 - \Delta n_2 + \Delta n_3 - \Delta n_4 = 0$.

2. Matrix representation

In addition to the complex rotation (see Sec. II B), we use a dilation by a positive real number α, given by the unitary operator [59]

$$D_\alpha = \exp\left(i \log(\alpha) \frac{\boldsymbol{r}\cdot\boldsymbol{p} + \boldsymbol{p}\cdot\boldsymbol{r}}{2}\right). \tag{15}$$

Under complex rotation (2) and dilation (15), the Cartesian coordinates and momenta transform as

$$\boldsymbol{r} \to \alpha \boldsymbol{r} e^{i\theta}, \quad \boldsymbol{p} \to \frac{1}{\alpha} \boldsymbol{p} e^{-i\theta}. \tag{16}$$

After complex rotation and dilation, the matrix representation of the generalized eigenvalue problem (10) reads

$$\mathbf{H}_0^\alpha(\theta)\boldsymbol{\Psi}_\theta = E_\theta \mathbf{J} \boldsymbol{\Psi}_\theta, \tag{17}$$

where

$$\mathbf{H}_0^\alpha(\theta) = -\frac{1}{2\alpha^2}\mathbf{T} e^{-2i\theta} + \frac{1}{\alpha}\mathbf{V} e^{-i\theta}, \tag{18}$$

with $\mathbf{T}$, $\mathbf{V}$, and $\mathbf{J}$ the matrix representations of (11), (12), and (9), respectively, and $\boldsymbol{\Psi}_\theta$ is the vector representation of the wave function.

3. Construction of the basis

The planar helium atom is invariant under rotations around an axis perpendicular to the plane, under the exchange symmetry P_{12} and under the parity Π. The system is also invariant under the reflections Π_x $(x_1, y_1, x_2, y_2) \to (x_1, -y_1, x_2, -y_2)$ and Π_y $(x_1, y_1, x_2, y_2) \to (-x_1, y_1, -x_2, y_2)$, which are related to the total parity by $\Pi = \Pi_x \Pi_y = \Pi_y \Pi_x$. These symmetries commute with L_z^2 and anticommute with L_z. In this paper the eigenstates of the planar helium atom are labeled by the absolute value $|l|$ of the angular momentum L_z, the exchange symmetry P_{12}, and the symmetry $\Pi_x = \pm 1$.

The symmetrization of the basis (14) with respect to P_{12} and L_z is given by [43,57]

$$|n_1 n_2 n_3 n_4\rangle^+ = |n_1 n_2 n_3 n_4\rangle + |n_3 n_4 n_1 n_2\rangle. \tag{19}$$

Additionally, the basis can be adapted to the symmetry Π_x by the definition [43,44]

$$|n_1 n_2 n_3 n_4\rangle^{+\epsilon_x} = |n_1 n_2 n_3 n_4\rangle^{+} + \epsilon_x |n_2 n_1 n_4 n_3\rangle^{+}, \tag{20}$$

where $\epsilon_x = \pm 1$. With this, the basis decomposes into the subspaces of even ($\epsilon_x = 1$) or odd ($\epsilon_x = -1$) states with respect to the symmetry Π_x, and of singlet and triplet states according to

$$\text{singlet states:} \quad n_1 - n_2 \equiv n_3 - n_4 \equiv 0 \ (\text{mod } 4);$$
$$\text{triplet states:} \quad n_1 - n_2 \equiv n_3 - n_4 \equiv 2 \ (\text{mod } 4).$$

The numerical implementation requires the truncation of the infinite symmetrized basis, which is made according to

$$n_1 + n_2 + n_3 + n_4 \leqslant n_{\text{base}}, \tag{21}$$

with n_{base} a positive integer. This value determines the dimensions of the matrices $\mathbf{H}_0^{\alpha}(\theta)$ and $\mathbf{J}$ in Eq. (17) which, due to the selection rules in (n_1, n_2, n_3, n_4), correspond to sparse banded matrices of bandwidth n_{larg} and size n_{tot}.

D. Helium atom under periodic driving

Now we consider the helium atom in presence of an external electromagnetic field. In the dipole approximation, with length gauge, and neglecting relativistic effects, the Hamiltonian for the driven atom reads

$$H = H_0 + F(x_1 + x_2)\cos(\omega t). \tag{22}$$

Here, H_0 is the unperturbed Hamiltonian (1) and the field is linearly polarized along the x direction and periodic in time with amplitude F and frequency ω.

Floquet theory

Since the Hamiltonian (22) is periodic in time, with period $T = 2\pi/\omega$, the Floquet theorem [48,49] guarantees that the solutions of the time-dependent Schrödinger equation

$$i\frac{\partial}{\partial t}|\psi(t)\rangle = H|\psi(t)\rangle \tag{23}$$

can be expressed as a superposition of time-periodic wave functions

$$|\psi(t)\rangle = \sum_i c_i e^{-i\varepsilon_i t}\big|\phi_{\varepsilon_i}(t)\big\rangle, \quad \big|\phi_{\varepsilon_i}(t+T)\big\rangle = \big|\phi_{\varepsilon_i}(t)\big\rangle,$$

where ε_i and $|\phi_{\varepsilon_i}(t)\rangle$ are the eigenvalues and eigenstates of the Floquet Hamiltonian $\mathcal{H}_F = H - i\frac{\partial}{\partial t}$, called *quasienergies* and *Floquet states*, respectively.

The Floquet states are periodic in time; therefore, they can be expanded in Fourier series:

$$\big|\phi_{\varepsilon_i}(t)\big\rangle = \sum_{k=-\infty}^{\infty} e^{-ik\omega t}\big|\phi_{\varepsilon_i}^k\big\rangle. \tag{24}$$

In this way, the eigenvalue problem $\mathcal{H}_F|\phi_{\varepsilon_i}(t)\rangle = \varepsilon_i|\phi_{\varepsilon_i}(t)\rangle$ reduces to

$$(H_0 - k\omega)\big|\phi_{\varepsilon_i}^k\big\rangle + \mathcal{F}\big(\big|\phi_{\varepsilon_i}^{k+1}\big\rangle + \big|\phi_{\varepsilon_i}^{k-1}\big\rangle\big) = \varepsilon_i\big|\phi_{\varepsilon_i}^k\big\rangle, \tag{25}$$

where

$$\mathcal{F} = \frac{F}{2}(x_1 + x_2). \tag{26}$$

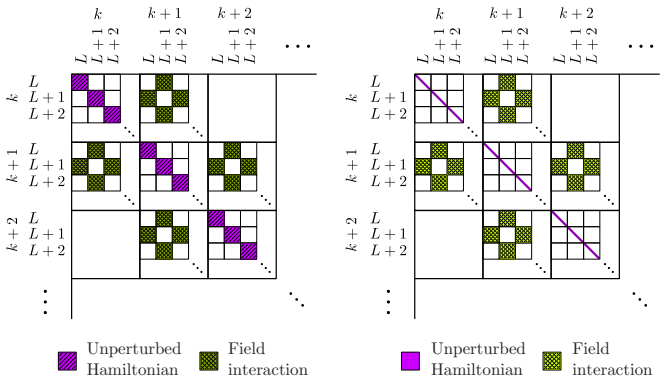

FIG. 1. Schematic block structure of the Hamiltonian matrices $\mathbf{A}$ (left) of the eigenvalue problem (27) and $\tilde{\mathbf{A}}$ (right) of the eigenvalue problem (31).

With the Floquet method, the time dependence has been eliminated, and we have a new quantum number k. In the limit of a large number of photons, there is a one-to-one correspondence between the quasienergy spectrum of the Floquet Hamiltonian and the energy spectrum of an atom dressed by a quantized field [49,60]. The number of photons exchanged between the atom and the field is then given by the Floquet quantum number k.

III. NUMERICAL TREATMENT

In Sec. II D, we show that, using Floquet theory, the TDSE (23) which describes the helium atom under periodic driving can be written as the eigenvalue problem (25), where the time dependence was eliminated and a new quantum number k was introduced. The matrix representation of Eq. (25) is given by

$$\mathbf{A}\Phi_i = \varepsilon_i\Phi_i, \quad \mathbf{A} = \mathbf{H}_0 - k\omega\mathbb{1} + \mathbf{F}, \tag{27}$$

with Φ_i the column vector representing $|\phi_i^k\rangle$ and $\mathbf{F}$ the matrix representation of (26).

The general form of matrix $\mathbf{A}$ is depicted in Fig. 1 (left). The matrix $\mathbf{H}_0$ is symmetric and has a block-diagonal structure. On the other hand, the matrix $\mathbf{F}$ is symmetric in the position gauge but it is antisymmetric in the velocity gauge, with a block structure where only elements for which $\Delta L = \pm 1$ and $\Delta k = \pm 1$ are coupled.

The numerical implementation requires a truncation in the number of Floquet blocks and angular momenta included in the computation according to

$$k_{\min} \leqslant k \leqslant k_{\max}, \quad L = 0, \ldots, L_{\max}. \tag{28}$$

In previous investigations [44], Eq. (27) has been solved directly in the harmonic oscillator basis (20). In that basis, the block matrix $\mathbf{H}_0$ has only a few terms different from zero due to the selection rules in (n_1, n_2, n_3, n_4). However, even for a small number of Floquet blocks and a low value of $L_{\max}$, the computations are time and memory consuming due to the large size of the matrix $\mathbf{A}$ [44,61]. As a consequence, it was not possible to provide a full picture of the NDWPs or their decaying properties. For instance, for $n_{\text{base}} = 200$, $k_{\min} = -2$, $k_{\max} = 4$, and $L_{\max} = 3$ the matrix size is $n_{\text{tot}} = 521\,795$,

while the RAM necessary to store the matrices is of the order of 430 GB.

Time-dependent Schrödinger equation in the atomic basis

Let us consider the atomic states $|\varphi_i^L\rangle$ which satisfy the time-independent Schrödinger equation

$$H_0|\varphi_i^L\rangle = \epsilon_i^L|\varphi_i^L\rangle, \tag{29}$$

where H_0 is the unperturbed Hamiltonian (1) and L is the total angular momentum. The solution to this equation is achieved with the approach described in Sec. II C.

Once we have obtained the states $|\varphi_i^L\rangle$, we can define the atomic basis adapted to solve the eigenvalue problem (25) by

$$\{|\varphi_i^{L,k}\rangle\}, \quad |\varphi_i^{L,k}\rangle = |k\rangle \otimes |\varphi_i^L\rangle, \tag{30}$$

where the identification of the Floquet quantum number k with the number of photons exchanged between the atom and the field discussed in Sec. II D allows us to write the above tensor product.

In the basis (30), the eigenvalue problem (27) writes

$$\tilde{\mathbf{A}}\tilde{\Phi}_i = \varepsilon_i\tilde{\Phi}_i, \quad \tilde{\mathbf{A}} = \mathbf{h}_0 - k\omega\mathbb{1} + \tilde{\mathbf{F}}, \tag{31}$$

where $\tilde{\Phi}_i$ is the solution vector in the atomic basis, $\mathbf{h}_0$ is the diagonal matrix containing the eigenvalues of $\mathbf{H}_0$, and the matrix $\tilde{\mathbf{F}}$—which has the same structure as $\mathbf{F}$—contains the dipole matrix elements $\langle\varphi_n^L|(x_1+x_2)|\varphi_m^{L+\Delta L}\rangle$, $\Delta L = \pm 1$. The general form of the matrix $\tilde{\mathbf{A}}$ is shown in Fig. 1 (right).

The diagonalization of both the unperturbed system (29) and the Floquet eigenvalue problem (31) is performed using an efficient implementation of the Lanczos algorithm [62,63].

The principal features of this method, as we will see in Sec. VII, are the tremendous reduction in the size of the matrices (with all the benefits that this entails from the computational point of view) and the possibility to identify the atomic states involved in the formation of NDWPs, which allows us to reduce the system to its very basic ingredients.

IV. UNPERTURBED FROZEN PLANET STATES

A. Classical frozen planet configuration

The classical FPC is a collinear and asymmetric configuration where both electrons are located on the same side of the nucleus. In this highly asymmetric configuration, which is dynamically stable [27,39,64], the inner electron precesses on highly eccentric ellipses and the outer electron remains nearly "frozen" around some equilibrium distance.

The phase space of the frozen planet configuration presented in Fig. 2 is visualized within a Poincaré surface of a section obtained by plotting the position x_1 and the momentum p_1 of the outer electron every time the inner electron reaches the nucleus. The numerical computation of the classical dynamics is achieved by the previous regularization of the equations of motion by Kustaanheimo-Stiefel transformations [65,66].

Within the formalism of adiabatic invariants [67], the fast Kepler oscillations of the inner electron define an effective attractive potential which describes the dynamics of the outer electron. From the shape of this potential, we can extract the intrinsic frequency and amplitude scales which determine the

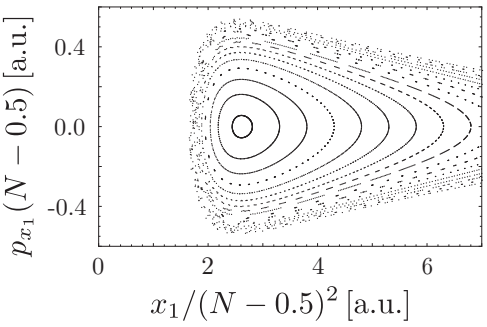

FIG. 2. Phase space of the outer electron in the collinear frozen planet configuration.

effect of an external driving field on the configuration [42,68]. The position $x_{\min}$ of the minimum of the effective potential, the minimum energy $E_{\min}$, the intrinsic frequency scale ω_I, and the intrinsic field strength F_I for the FPC, in atomic units, are

$$\begin{aligned} x_{\min} &= 2.6S^2, \quad \omega_I = 0.3S^{-3}, \\ E_{\min} &= -2.22S^{-2}, \quad F_I = 0.03S^{-4}, \end{aligned} \tag{32}$$

where $S = \frac{1}{2\pi}\oint p_2 dx_2$ is the action integral over one cycle of the Kepler oscillation of the inner electron, with x_2 and p_2 its position and momentum, respectively. The natural scale F_I for the field strength is given by the maximum slope of the effective potential and defines the minimum static field necessary to ionize the configuration. The frequency scale ω_I is given by the curvature of the potential at its minimum. This is the frequency of small oscillations around the equilibrium position.

In a quantum description, the action S is replaced by the effective quantum number of the inner electron N, and the scaled quantities (32) take the form

$$x_{\min} = 2.6(N-\delta)^2, \tag{33}$$

$$\omega_I = 0.3(N-\delta)^{-3}, \tag{34}$$

$$E_N = -2.22(N-\delta)^{-2}, \tag{35}$$

$$F_I = 0.03(N-\delta)^{-4}, \tag{36}$$

where $\delta = 0.5$ [57] and $\delta = 0$ for two-dimensional (2D) and 3D helium, respectively.

The existence of FPSs (which are the quantum counterparts of the FPCs) have been demonstrate theoretically on 1D [42], 2D [44,46], and 3D [40] helium for $N \geqslant 3$. However, these states have so far not been unambiguously identified in experiments, though sequential multiphoton excitation schemes [69–71] have successfully been used for the creation of planetary states [25] where highly excited electrons move in different regions of space($\langle \boldsymbol{r}_2\rangle < \langle \boldsymbol{r}_1\rangle$).

B. Identification of frozen planet states

Frozen planet states are localized along a collinear configuration, thus for these states the expectation value of the cosine of the angle θ_{12} between the two electrons has to be close to unity ($\langle\cos\theta_{12}\rangle \simeq 1$). In addition, FPSs have long lifetimes compared to other resonances in the same energy regime. In this way, we can use the decay rates and the expectation

value of $\cos\theta_{12}$ to identify quantum states along classical frozen planet trajectories in helium spectra. However, these two quantities do not fully characterize the FPS, and their unambiguous identification also requires the study of the localization properties of the electronic density in configuration space and phase space.

Due to the high dimensionality of the configuration and phase spaces, the visualization of the wave function requires the use of projections of the probability density. The visualization in configuration space is achieved using conditional probability distributions for $\theta_{12} = 0$ or one-electron probability densities. In the frame of complex rotation the full probability density for an isolated resonance of complex energy E_j takes the form [44,72]

$$|\psi(\boldsymbol{r})|^2 \simeq \frac{1}{\pi|\mathrm{Im}\, E_j|}\mathrm{Re}\,\langle \boldsymbol{r}|R(-\theta)|\Psi_{j,\theta}\rangle^2, \tag{37}$$

where $\boldsymbol{r} = (\boldsymbol{r}_1, \boldsymbol{r}_2)$.

The electronic density of a FPS of energy E_j can also be projected into the phase space with the help given by the Husimi function [42,44]:

$$W_{\phi_E}(q,p) \simeq \frac{1}{\pi|\mathrm{Im}\, E_{j,\theta}|}\mathrm{Re}\int d\boldsymbol{r}\,\phi_{q,p}(\boldsymbol{r})\langle \boldsymbol{r}|R(-\theta)|\Psi_{j,\theta}\rangle \times \int d\boldsymbol{r}'\,\phi^*_{q,p}(\boldsymbol{r}')\langle \boldsymbol{r}'|R(-\theta)|\Psi_{j,\theta}\rangle, \tag{38}$$

with $\phi_{q,p}$ the modified coherent state

$$\phi_{q,p}(\boldsymbol{r}) = \exp\left(-\tfrac{1}{2}\omega_s(x_1-q)^2 - ix_1p\right) \times \delta\left(x_2 - x_2^0\right)\delta(y_1)\delta(y_2), \tag{39}$$

centered at the point (p, q) in the phase space. Here, $x_2^0 \simeq 0$ and $\omega_s \simeq \omega_I = 0.3(N-1/2)^{-3}$, i.e., the intrinsic frequency of the FPC.

Finally, the expectation value of $\cos\theta_{12}$ for a resonance state $|\Psi_{j,\theta}\rangle$ is calculated with the help of the expression [44]

$$\langle\cos\theta_{12}\rangle \simeq \frac{1}{\pi|\mathrm{Im}\, E_{j,\theta}|}\mathrm{Re}\langle\overline{\Psi_{j,\theta}}|\cos\theta_{12}|\Psi_{j,\theta}\rangle. \tag{40}$$

V. FROZEN PLANET STATES OF 2D HELIUM

Our principal interest is to study frozen planet states of helium under near-resonant driving. In this direction, the first step is to identify the FPS in the spectrum of the unperturbed atom. Frozen planet states are organized in series converging to single ionization thresholds I_N and will here be denoted by $\mathcal{F}^N_{n_\mathrm{F}}$, where N corresponds to the principal quantum number of the inner electron and n_F indicates the position of the FPS in the series.

We diagonalize the unperturbed Hamiltonian H_0 in the energy region below the $N = 3, \ldots, 7$ ionization thresholds for angular momentum $L = 0$ and 1. In the obtained energy spectrum, we identify the lowest FPS of the series converging to each ionization threshold. In Table I we present the energies of the ground ($n_\mathrm{F} = 1$) FPS compared with the semiclassical values obtained by Eq. (35). As N increases, quantum results are closer to the semiclassical energies. This is not surprising since the semiclassical regime of the Coulomb potential is located at energies close to the double ionization threshold

TABLE I. Energies of the ground ^1S and ^3S frozen planet states for $N = 3, \ldots, 7$ in planar helium. The semiclassical values E_N are obtained from Eq. (35). Notice that the semiclassical energy (35) does not account for the zero-point energy of the effective potential. This can be done with the help of the EKB quantization [39]. This, however, does not improve the results presented in this table.

N	$-E_N$ (a.u.)	$-E(^1S)$ (a.u.)	$-E(^3S)$ (a.u.)
3	0.355 20	0.354 907 546	0.352 128 587
4	0.181 22	0.180 560 506	0.180 360 430
5	0.109 63	0.109 297 551	0.109 260 500
6	0.073 39	0.073 207 046	0.073 203 013
7	0.052 54	0.052 445 661	0.052 443 726

[73,74]. In addition, the singlet-triplet energy splitting due to particle exchange effects which are not considered in the semiclassical prediction decreases exponentially with N [46].

We calculate the energies, decay rates, and $\langle\cos\theta_{12}\rangle$ for the first four singlet (Table II) and triplet (Table III) 2D frozen planet states for $L = 0, 1$ and $N = 3, \ldots, 7$. For $N \geqslant 5$ the $L = 0$ FPSs possess small decay rates and largest value of $\langle\cos\theta_{12}\rangle$ compared with the $L = 1$ FPS. We observe also that $\langle\cos\theta_{12}\rangle$ increases with N and n_F, consistent with the semiclassical character of the highly doubly excited states.

In the left panels of Fig. 3 we present the conditional ($\theta_{12} = 0$) probability density [77] of the lowest ^1S FPS below the $N = 4$ single ionization threshold. The inner electron labeled by the index 2 is close to the nucleus while the outer electron labeled by the index 1 is far from the nucleus. For the ground FPS, the maximum of the probability density is localized near the equilibrium position x_min of the outer electron in the classical configuration given by Eq. (33). In the case of the excited FPS, the maximum of the probability density along the inner electron axis remains at the same position whereas the maximum along the outer electron axis increases with n_F.

The correspondence of these states with the classical frozen planet configuration is more evident from the plots on the right side of Fig. 3. Each of these plots is composed of two parts. The left part corresponds to the inner electron density for a fixed position of the outer electron, while the right part shows the outer electron density for a fixed position of the inner electron. The value for the position of the fixed electron is given by the maximum of the conditional probability density for the respective electron.

Figure 4 displays the Husimi distributions of the first four ^1S FPSs converging to the sixth series for planar helium. Comparing these plots with the phase space of classical configuration in Fig. 2, we observe that the maximum of the probability density of the ground state is localized at the equilibrium position of the outer electron in the classical FPC given by Eq. (33). On the other hand, excited FPSs are localized along periodic orbits with higher energy of the classical configuration.

VI. DRIVEN FROZEN PLANET CONFIGURATION

In the presence of an external time-periodic electromagnetic field, the dynamics of the collinear frozen planet con-

TABLE II. Energies, decay rates, and $\langle\cos\theta_{12}\rangle$ for the four lowest ^1S and ^1P frozen planet states for $N = 3, \ldots, 7$ in planar helium.

N	n_F	$-E$ (a.u.)	$\Gamma/2$ (a.u.)	$\langle\cos\theta_{12}\rangle$
		^1S states		
3	1	0.354 907 546	0.000 003 373	0.672
	2	0.342 496 485	0.000 0004 76	0.676
	3	0.335 495 095	0.000 000 073	0.680
	4	0.331 264 862	0.000 000 071	0.681
4	1	0.180 560 506	0.000 000 877	0.788
	2	0.175 705 103	0.000 001 483	0.785
	3	0.172 615 385	0.000 001 593	0.782
	4	0.170 535 543	0.000 001 452	0.781
5	1	0.109 297 551	0.000 003 748	0.772
	2	0.106 832 792	0.000 000 062	0.853
	3	0.105 139 500	0.000 000 179	0.862
	4	0.103 925 428	0.000 000 337	0.864
6	1	0.073 207 046	0.000 010 180	0.950
	2	0.071 801 931	0.000 006 145	0.902
	3	0.070 770 672	0.000 002 634	0.884
	4	0.069 994 857	0.000 001 482	0.882
7	1	0.052 445 661	0.000 001 443	0.888
	2	0.051 561 367	0.000 002 240	0.894
	3	0.050 887 178	0.000 001 949	0.895
	4	0.050 361 468	0.000 001 562	0.898
		^1P states		
3	1	0.348 950 783	0.000 000 088	0.616
	2	0.338 858 835	0.000 000 055	0.608
	3	0.333 238 049	0.000 000 035	0.599
	4	0.329 797 285	0.000 000 024	0.591
4	1	0.179 248 594	0.000 001 534	0.693
	2	0.174 807 889	0.000 001 010	0.691
	3	0.171 980 605	0.000 000 669	0.690
	4	0.170 073 973	0.000 000 465	0.688
5	1	0.108 773 791	0.000 005 206	0.680
	2	0.106 479 587	0.000 002 816	0.716
	3	0.104 884 000	0.000 002 000	0.732
	4	0.103 734 973	0.000 001 206	0.741
6	1	0.073 044 134	0.000 002 573	0.818
	2	0.071 713 237	0.000 007 305	0.762
	3	0.070 726 659	0.000 009 997	0.722
	4	0.069 972 887	0.000 010 269	0.703
7	1	0.052 351 581	0.000 000 361	
	2	0.051 498 957	0.000 001 302	0.867
	3	0.050 846 645	0.000 003 033	0.848
	4	0.050 336 417	0.000 004 942	0.823

TABLE III. Energies, decay rates, and $\langle\cos\theta_{12}\rangle$ for the four lowest ^3S and ^3P frozen planet states for $N = 3, \ldots, 7$ in planar helium. In the case of $N = 4$ only two ^3S FPSs have been identified.

N	n_F	$-E$ (a.u.)	$\Gamma/2$ (a.u.)	$\langle\cos\theta_{12}\rangle$
		^3S states		
3	1	0.352 128 587	0.000 001 529	0.427
	2	0.340 903 255	0.000 001 835	0.468
	3	0.334 395 783	0.000 000 992	0.531
	4	0.330 517 901	0.000 000 601	0.563
4	1	0.180 360 430	0.000 000 418	0.760
	2	0.175 457 936	0.000 001 558	0.613
5	1	0.109 260 500	0.000 000 021	0.839
	2	0.106 794 314	0.000 000 037	0.838
	3	0.105 099 702	0.000 000 046	0.835
	4	0.103 887 667	0.000 000 049	0.832
6	1	0.073 203 013	0.000 000 006	0.869
	2	0.071 788 666	0.000 000 007	0.871
	3	0.070 756 000	0.000 000 007	0.872
	4	0.069 980 757	0.000 000 007	0.872
7	1	0.052 443 726	0.000 000 130	0.888
	2	0.051 557 442	0.000 000 088	0.891
	3	0.050 882 036	0.000 000 065	0.893
	4	0.050 355 907	0.000 000 049	0.895
		^3P states		
3	1	0.349 389 074	0.000 000 130	0.690
	2	0.339 211 003	0.000 000 135	0.726
	3	0.333 485 926	0.000 000 101	0.745
	4	0.329 971 022	0.000 000 072	0.755
4	1	0.179 424 139	0.000 008 708	0.775
	2	0.174 965 590	0.000 001 044	0.801
	3	0.172 105 472	0.000 000 312	0.818
	4	0.170 170 487	0.000 000 143	0.829
5	1	0.108 873 521	0.000 006 070	0.776
	2	0.106 618 280	0.000 007 045	0.585
	3	0.104 979 719	0.000 003 584	0.777
	4	0.103 806 525	0.000 001 699	0.821
6	1	0.073 024 843	0.000 003 008	0.836
	2	0.071 671 979	0.000 006 616	0.833
	3	0.070 675 246	0.000 009 262	0.780
7	1	0.052 349 313	0.000 001 742	0.657
	2	0.051 493 345	0.000 003 555	0.881
	3	0.050 837 398	0.000 004 744	0.892
	4	0.050 324 264	0.000 004 666	0.887

figuration takes place in a five-dimensional phase space described by the positions and momenta of the electrons, and by the phase ωt of the driving field.

For near-resonant driving $\omega \approx \omega_I = 0.3(N-0.5)^{-3}$ of amplitude $F < F_I = 0.03(N-0.5)^{-4}$, which do not affect in a sensitive way the frozen planet dynamics, the time scale separation between the fast Kepler oscillations of the inner electron and the slow motion of the outer electron makes it possible to map the phase-space structure onto a two-dimensional surface by a two-step Poincaré section method [41,64]. The first Poincaré section is obtained by plotting the position x_1 and momentum p_1 of the outer electron each time the inner electron hits the nucleus at $x_2 = 0$. The resulting points, which describe the slow outer electron's oscillation, are connected by cubic interpolation to construct a continuous trajectory, used to perform a second Poincaré section by fixing the phase of the driving field $\omega t = \phi_0 \,(\mathrm{mod}\, 2\pi)$.

In Fig. 5 is depicted the two-step Poincaré surface of a section obtained for fixed field frequency $\omega = 0.2(N-0.5)^{-3}$ a.u. and different field amplitudes. In the left plot, the field amplitude is $F = 0$. For field amplitude $F = 0.001(N-0.5)^{-4}$ a.u. (middle) the phase space becomes mixed with

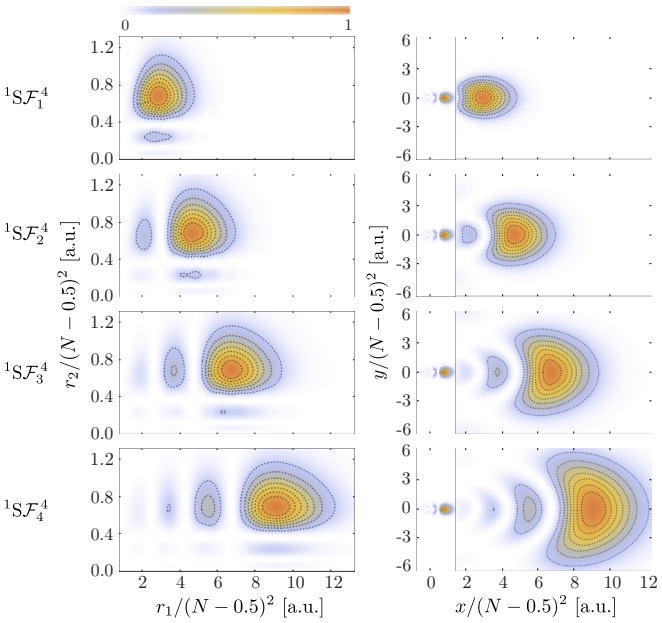

FIG. 3. Left: Conditional probability density ($\theta_{12} = 0$) of the lowest ^1S frozen planet states of the $N = 4$ series in planar helium. For the ground FPS, the maximum of the probability density is localized near the equilibrium position x_{min} of the outer electron in the classical configuration [Eq. (33)]. For the excited FPS, the maximum of the probability density along the inner electron axis r_2 remains at the same position while the maximum along the outer electron axis r_1 increases with n_{F}. Right: Projections in configuration space for the electronic density of the ^1S, $N = 4$ frozen planet states. In each plot, the left part corresponds to the inner electron density for a fixed position of the outer electron, while the right part shows the outer electron density for a fixed position of the inner electron. The value for the position of the fixed electron is given by the maximum of the corresponding conditional probability density displayed in the left panels.

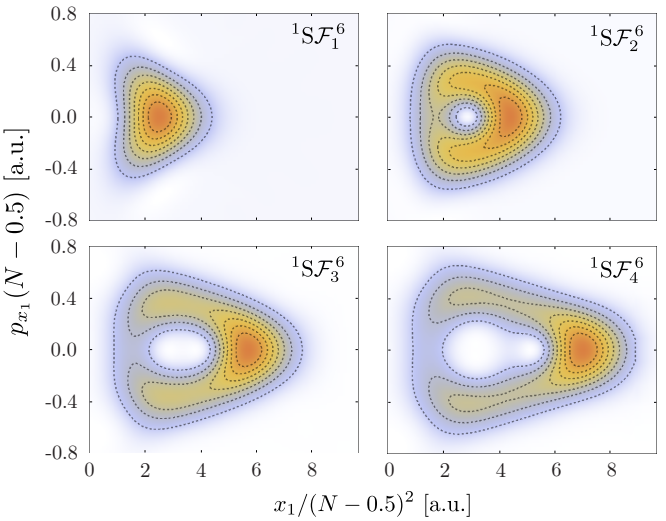

FIG. 4. Projections in phase space for the electronic density of the ^1S frozen planet states of the $N = 6$ series in planar helium. For the ground FPS $^1S\mathcal{F}_1^6$ the maximum of the probability density is localized at the equilibrium position of the outer electron in the classical FPC shown in Fig. 2, while for the excited FPS the maximum of the probability density is localized along periodic orbits with higher energy of the classical configuration.

regular and chaotic regions. At the position $x_1 = 4.8(N - 0.5)^2$ a.u., we can identify a substructure which corresponds to the 1:1 resonance. At larger field amplitude, $F = 0.005(N - 0.5)^{-4}$ a.u. (right), the induced resonance separates from the rest of the regular domain and the phase space exhibits two regular islands: the *intrinsic* island and the *resonance* island, which are embedded into the chaotic sea and are localized at the positions $x_1 = 2.5(N - 0.5)^2$ a.u. and $4.9(N - 0.5)^2$ a.u., respectively.

Figure 6 shows the classical phase-space structure for field amplitude $F = 0.005(N - 0.5)^{-4}$ a.u. and frequency $\omega = 0.2(N - 0.5)^{-3}$ a.u., for three different field phases ωt. The intrinsic island remains basically unaffected by the field while the resonance island oscillates around the intrinsic island with the same field frequency.

VII. NONDISPERSIVE WAVE PACKETS IN 2D HELIUM

A. Identification of NDWPs below the sixth ionization threshold

In this section, we study doubly excited states of planar helium under periodic driving. The main interest is to verify the applicability of the method presented in Sec. III to investigate driven frozen planet states and to identify nondispersive wave packets in helium.

There is evidence for the existence of nondispersive wave packets in the energy region below the $N = 6$ ionization threshold of planar helium [44]. Hence, we start our study of driven frozen planet states precisely in that energy region, with special attention on the lowest triplet (^3S) FPS of the $N = 6$ series (Table III). The same analysis presented in this section leads to the description of NDWPs for other symmetries and ionization thresholds. The results are discussed in Sec. VII D.

As mentioned in Sec. III, our approach is based on two principal steps. First, we diagonalize the unperturbed Hamiltonian for $L = 0, \ldots, L_{\text{max}}$ (each one of these calculations is performed independently since for the unperturbed atom the angular momentum is a conserved quantity). Figure 7 displays the complex spectrum for triplet states converging to the sixth ionization threshold obtained by diagonalization of Eq. (17), for $n_{\text{base}} = 250$ and $L = 0, \ldots, 7$.

In the second step, the numerical investigation of the driven atom is achieved by solving the eigenvalue problem (31). The matrix to diagonalize is expressed in the atomic basis

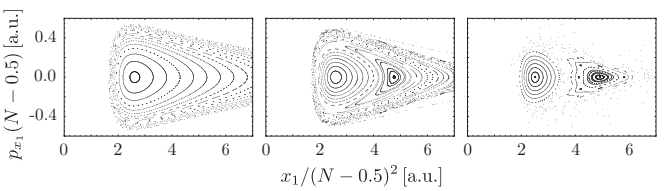

FIG. 5. Phase space of the driven frozen planet configuration for fixed field frequency $\omega = 0.2(N - 0.5)^{-3}$ a.u. and three different field amplitudes: $F = 0$ a.u. (left), $F = 0.001(N - 0.5)^{-4}$ a.u. (center), and $F = 0.005(N - 0.5)^{-4}$ a.u. (right).

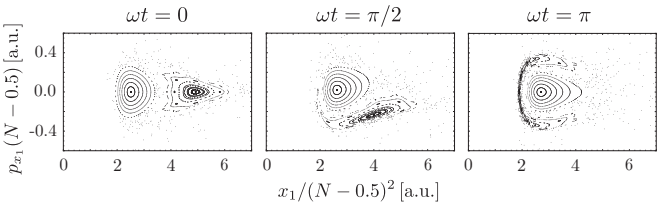

FIG. 6. Phase space of the driven frozen planet configuration for field amplitude $F = 0.005(N-0.5)^{-4}$ a.u., frequency $\omega = 0.2(N-0.5)^{-3}$ a.u., and variable driving field phases ωt.

(30), which is built up using the states in Fig. 7 and 15 Floquet blocks ($k_{\min} = -7$ and $k_{\max} = 7$), i.e., we study the dynamics of the atomic states obtained in the previous step, under the action of the external field. For the electromagnetic driving, we use the field frequency $\omega = 0.0012$ a.u. and field amplitude $F = 5.5 \times 10^{-6}$ a.u., which induces the well-pronounced 1:1 resonance and intrinsic island in the classical phase space in Fig. 5 (right). The result was tested for convergence by repeating the calculations for atomic bases obtained with different values of the complex rotation angle θ and the dilation parameter α.

The Floquet eigenstates obtained by diagonalization of Eq. (31) are given by a superposition of atomic states. Hence, we can identify the states for which the greatest contribution in the atomic basis is given by a FPS $\mathcal{F}_j^N$, i.e., the Floquet states $|\psi\rangle$ with the largest overlap $|\langle \mathcal{F}_j^N|\psi\rangle|^2$. We denote them by $\mathcal{W}_j^N$.

Figure 8 shows the projected Husimi distributions of the Floquet eigenstates with the largest overlap with the lowest ^3S FPS in the sixth series of the field-free atom. The state $\mathcal{W}_1^6$ follows the same oscillation of the intrinsic island in the classical structure (bottom). On the other hand, the states $\mathcal{W}_2^6$ and $\mathcal{W}_3^6$, anchored to the hyperbolic and elliptic fixed points of the 1:1 resonance, respectively, oscillate around the intrinsic island with the same field frequency.

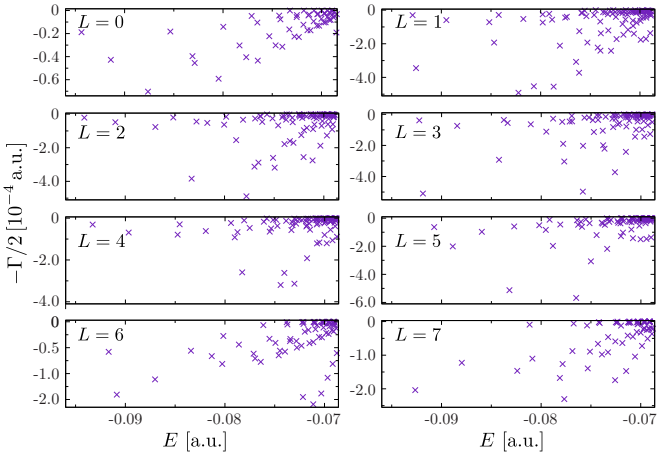

FIG. 7. Complex energy spectrum of the unperturbed helium atom for triplet states in the energy region below the sixth ionization threshold, obtained after diagonalization of (17) for $n_{\text{base}} = 250$ and several angular momenta.

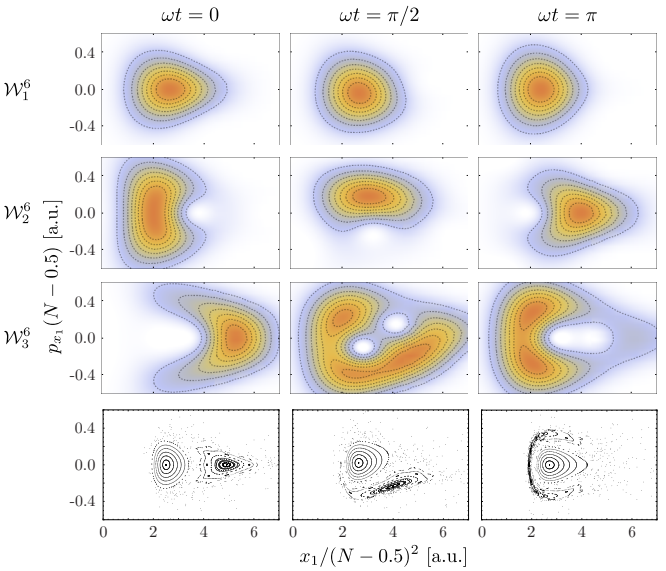

FIG. 8. Husimi distributions of the triplet wave packets $\mathcal{W}_1^6$, $\mathcal{W}_2^6$, and $\mathcal{W}_3^6$ obtained for field parameters $F = 5.5 \times 10^{-6}$ a.u. and $\omega = 0.0012$ a.u., depicted for different phases of the driving field. For comparison, we show the classical phase-space structure obtained for the same field parameters (bottom).

Figure 9 shows the electronic density in configuration space for the Floquet states $\mathcal{W}_1^6$, $\mathcal{W}_2^6$, and $\mathcal{W}_3^6$. In the three cases, we observe that the probability density of the inner electron is not affected by the field, while the probability density of the outer electron oscillates with the driving frequency.

The above results reproduce the dynamics of the nondispersive wave packets identified in Refs. [44,61], where, the dynamics of the lowest triplet ^3S FPS of the $N = 6$ series under periodic driving was studied by solving Eq. (25) for $k_{\min} = -2$, $k_{\max} = 4$, and $L_{\max} = 3$ in a harmonic oscillator basis of 521 795 elements. It is worth mentioning that, despite the large size of the basis used, they have not been able to obtain a converged value of the wave-packet decay rates, while we

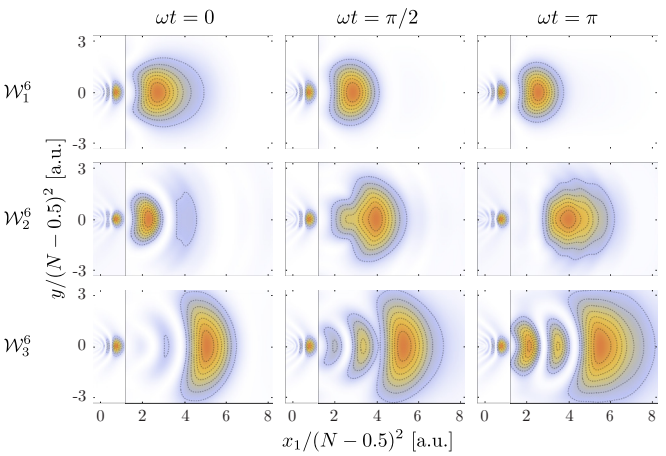

FIG. 9. Projections in configuration space of the electronic density of the same wave packets presented in Fig. 8. In each plot, the left part shows the inner electron density, while the right part shows the outer electron density.

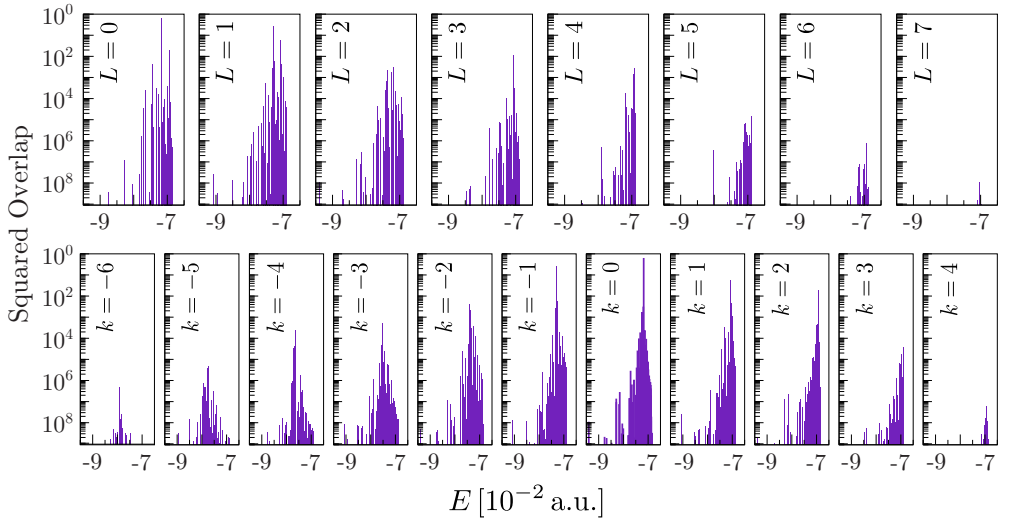

FIG. 10. Overlaps of the wave packet $\mathcal{W}_2^6$ with the states of the atomic basis organized according to angular momentum L (top) and the Floquet number k (bottom). Driving field parameters: $F = 5.5 \times 10^{-6}$ a.u. and $\omega = 0.0012$ a.u.

obtained converged values (presented in Table V) with a small basis of only 4366 elements (that is, approximately 100 states per angular momentum). One of the advantages of our method is that we can identify the atomic states that contribute to the formation of the NDWP. This will be clear in the next section.

B. Characterization of NDWPs below the sixth ionization threshold

In the previous section, we have seen that it is possible to study the dynamics of FPSs under electromagnetic driving in an efficient way, using an expansion in a basis set of a relatively small number of atomic eigenstates. Here, we study in more detail the NDWP identified in the previous section, with the aim of determining which of the atomic states have the most relevant participation in the process of formation of NDWPs in helium.

Following the notation introduced in Sec. VII A, we identify the Floquet eigenstates with the largest overlap with the lowest ^3S FPS in the sixth series of the field-free atom as $\mathcal{W}_j^6$. In order to quantify the contribution of the atomic eigenstates $|\varphi_i^{L,k}\rangle$ in the basis (30) to each wave packet $\mathcal{W}_j^6$, we calculate the overlaps $|\langle\varphi_i^{L,k}|\mathcal{W}_j^6\rangle|^2$, i.e., the square modulus of the components of the Floquet eigenstate $\mathcal{W}_j^6$. Here, we present our analysis for the wave packet $\mathcal{W}_2^6$. The results for the wave packets $\mathcal{W}_1^6$ and $\mathcal{W}_3^6$ are qualitatively similar.

Figure 10 shows the overlaps for the wave packet $\mathcal{W}_2^6$ and the basis elements for field amplitude $F = 5.5 \times 10^{-6}$ a.u. and frequency $\omega = 0.0012$ a.u. In the top plots, we observe, as expected, that the main contributions come from the atomic states with lower angular momentum. Unexpected is that only two states carry 90% of the weights: the Floquet state $\mathcal{W}_2^6$ exhibits the largest overlap with the frozen planet states $^3S\mathcal{F}_2^6$ (63%) and $^3P\mathcal{F}_1^6$ (27%). The contributions from other states are smaller and decrease rather fast by increasing L. In particular, the contributions from $L = 7$ angular momentum states are eight orders of magnitude smaller than for $L = 0$. Thus, we do not expect significant contribution for atomic states of angular momentum $L = 8$ or greater.

In the bottom panels of Fig. 10 the overlaps are organized according to the Floquet number k. The main contribution is given by the atomic states in the Floquet blocks from $k = -2$ to 2. In addition, we observe that the contribution from atomic states in the Floquet block $k = 4$ is seven orders of magnitude smaller than the one for $k = 0$, and contribution for $k = 5$ or greater is not expected since the number of photons to reach the sixth ionization threshold from the frozen planet state $^3S\mathcal{F}_2^6$ is 4.

In Fig. 11, we present the energies (left) and decay rates (right) of the Floquet spectrum as a function of the field amplitude F for fixed field frequency $\omega = 0.0012$ a.u. In the limit $F = 0$, the Floquet eigenstates correspond to unperturbed states with energy E shifted by $k\omega$. By increasing the field amplitude, the Floquet eigenstates are given by a superposition of atomic states and energy levels shift due to the repulsion between coupled Floquet states. Green, blue, and red circles identify the states $\mathcal{W}_1^6$, $\mathcal{W}_2^6$, and $\mathcal{W}_3^6$, respectively.

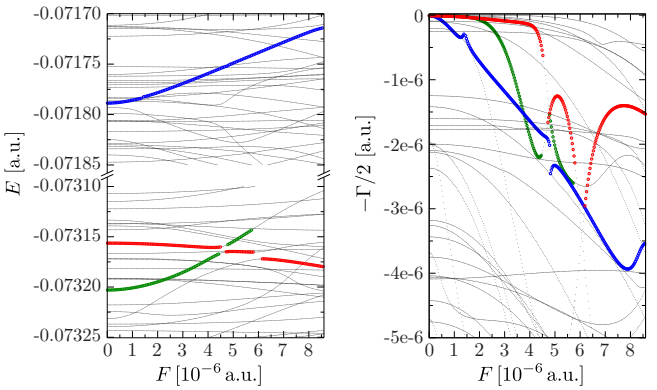

FIG. 11. Behavior of the energies E (left) and decay rates Γ (right) as a function of the field amplitude F, for driving frequency $\omega = 0.0012$ a.u. Green, blue, and red circles identify the wave packets $\mathcal{W}_1^6$, $\mathcal{W}_2^6$, and $\mathcal{W}_3^6$, respectively. For field amplitudes $F > 5.7 \times 10^{-6}$ a.u., there are no Floquet eigenstates with the largest overlap with the FPS $^3S\mathcal{F}_1^6$.

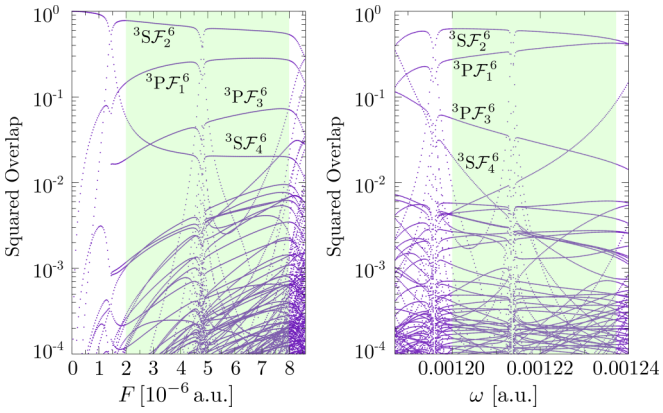

FIG. 12. Overlaps between the triplet wave packet $\mathcal{W}_2^6$ and the elements in the basis. The left plot shows the overlaps as a function of the field amplitude F for fixed frequency $\omega = 0.0012$ a.u., while in the right plot we present the overlaps as a function of the field frequency ω for a fixed amplitude $F = 5.5 \times 10^{-6}$ a.u. The green regions identify the field amplitude (left) and frequency (right) intervals for which the Husimi distribution of the wave packet $\mathcal{W}_2^6$ follows the classical trajectory as in Fig. 8.

In the left plot, for $F > 2 \times 10^{-6}$ a.u., the energies of the states $\mathcal{W}_1^6$ and $\mathcal{W}_2^6$ exhibit a pronounced shift at positive slope, which is associated to a large dipole moment of the electronic density in configuration space [78]. In the right plot, we show the imaginary part of the Floquet spectrum, which corresponds to half of the decay rates Γ. In this plot, we observe that the decay rate of the Floquet eigenstate $\mathcal{W}_3^6$ remains approximately constant for $F < 4 \times 10^{-6}$ a.u., and for field amplitudes around $F = 5 \times 10^{-6}$ and 7×10^{-6} a.u. the decay rate exhibits abrupt changes due to avoided crossings. For the case of the states $\mathcal{W}_1^6$ and $\mathcal{W}_2^6$, the decay rates show a pronounced shift at a negative slope. Thus, the tendency of these decay rates is to increase with the field amplitude.

Figure 12 shows the overlaps between the wave packet $\mathcal{W}_2^6$ and the elements in the basis for different field parameters. The green region identifies the intervals for the field amplitude (left) and frequency (right), where the Floquet state $\mathcal{W}_2^6$ exhibits the nondispersive behavior. To establish this region, we calculated the Husimi distributions of the triplet wave packet $\mathcal{W}_2^6$ for the different field parameters, verifying that the dynamics shown in Fig. 8 was reproduced. Similar results were observed for the wave packets $\mathcal{W}_1^6$ and $\mathcal{W}_3^6$. However, this is not conclusive, since by varying the field frequency (amplitude) the green region in the left (right) plot can change. Thus, the complete characterization of the wave-packet behavior in terms of the field parameters requires the simultaneous variation of F and ω.

In the left plot in Fig. 12, the overlaps are calculated as a function of the field amplitude F for fixed frequency $\omega = 0.0012$ a.u. There, we observe that in the limit $F = 0$ the overlap with the frozen planet state $^3S\mathcal{F}_2^6$ is equal to 1, which means that the Floquet state $\mathcal{W}_2^6$ has only one component in the atomic basis, given by the unperturbed state $^3S\mathcal{F}_2^6$. By increasing the field amplitude, the overlaps with the other elements in the basis become different from zero and in particular we observe that the principal contribution comes from the frozen planet states $^3S\mathcal{F}_2^6$, $^3P\mathcal{F}_1^6$, $^3P\mathcal{F}_3^6$, and $^3S\mathcal{F}_4^6$. The small perturbations observed for the values $F = 1.5 \times 10^{-6}$ and 4.8×10^{-6} a.u. correspond to avoided crossings between Floquet states (see Fig. 11). The right plot displays the overlaps as a function of the field frequency ω for fixed amplitude $F = 5.5 \times 10^{-6}$ a.u. Again, the main contribution to the wave packet is coming from a few S and P frozen planet states. For $\omega = 0.00124$ a.u., the contribution from the unperturbed states $^3S\mathcal{F}_2^6$ and $^3P\mathcal{F}_1^6$ is the same because this frequency corresponds to the resonant value $\omega = |E(^3S\mathcal{F}_2^6) - E(^3P\mathcal{F}_1^6)|$.

To conclude this section, let us remark that we have performed our computations employing only the resonances of the subseries converging to the $N = 6$ ionization threshold. To illustrate the fact that this basis is enough to study the formation of NDWPs, we repeated the computations including the resonances of $L = 0, \ldots, 8$ below the $N = 5, 6$, and 7 ionization thresholds with their respective continua and 51 Floquet blocks ($k_{\text{min}} = -25$ and $k_{\text{max}} = 25$) in the construction of the atomic basis (30). In that case, the number of basis elements was 114 319, which still remains smaller than the basis of 521 795 elements used in Ref. [44]. However, with the inclusion of more states on the basis we do not observe any improvement in the convergence for the wave-packet energies and decay rates, and the behavior of Figs. 11 and 12 remains the same. This was expected, since at least 22 photons are necessary to couple the frozen planet state $^3S\mathcal{F}_2^6$ to states below the fifth ionization threshold and 20 photons to reach the seventh ionization threshold. This supports the fact that in our initial calculation we actually include all the relevant states and that in the dynamics of the driven frozen planet states single ionization is the dominant decay process [44].

C. Few level model for NDWPs

The results in Fig. 10 suggest that by removing from the atomic basis (30) the states of negligible overlap with the wave packets $\mathcal{W}_1^6$, $\mathcal{W}_2^6$, and $\mathcal{W}_3^6$, and considering only a small number of Floquet blocks, the dynamics of the driven FPS should not be affected considerably. On the other hand, if we remove from the basis one of the atomic states with greater contribution to the wave packets, we wait for an observable modification of the wave-packet dynamics, i.e., in the electronic density projections in Figs. 8 and 9. In such a way, we can identify the atomic states that play a fundamental role in the formation of NDWPs in helium.

For this purpose, we remove progressively from the basis the resonances of the unperturbed atom with the lowest overlap with the wave packets $\mathcal{W}_1^6$, $\mathcal{W}_2^6$, and $\mathcal{W}_3^6$, in order to keep only the minimum number of atomic states and Floquet blocks that must be plugged into the model to reproduce the dynamics shown in Fig. 8. This procedure leaves us with the six atomic states in Table IV and Floquet blocks from $k_{\text{min}} = -1$ to $k_{\text{max}} = 2$. In other words, if we construct the basis (30) only with these six states for $k_{\text{min}} = -1$ to $k_{\text{max}} = 2$ and solve (31) for the field parameters $F = 5.5 \times 10^{-6}$ a.u. and $\omega = 0.0012$ a.u., we identify Floquet eigenstates $\mathcal{W}_1^6$, $\mathcal{W}_2^6$, and $\mathcal{W}_3^6$ that exhibit the same Husimi distributions displayed in Fig. 8.

In Table V column (b), we present the values for the energy and decay rate for the wave packets $\mathcal{W}_1^6$, $\mathcal{W}_2^6$, and

TABLE IV. Energies and decay rates of the atomic states needed to reproduce the dynamics of the wave packets $\mathcal{W}_2^6$, $\mathcal{W}_3^6$, and $\mathcal{W}_4^6$ presented in Sec. VII A. The state $\mathcal{G}_1^6$ corresponds to the ground state of a series of FPS-like states.

	^3S		^3P	
	$-E$ (a.u.)	$\Gamma/2$ (a.u.)	$-E$ (a.u.)	$\Gamma/2$ (a.u.)
$\mathcal{G}_1^6$			0.074 452 683	0.000 000 202
$\mathcal{F}_1^6$	0.073 203 013	0.000 000 006	0.073 024 843	0.000 003 008
$\mathcal{F}_2^6$	0.071 788 666	0.000 000 007	0.071 671 979	0.000 006 616
$\mathcal{F}_3^6$	0.070 756 000	0.000 000 007		

$\mathcal{W}_3^6$ obtained with the *few level model* [79]. The values for the energy obtained with the atomic basis of 4366 elements of Sec. VII A and the few level model in columns (a) and (b), respectively, are the same up to the fourth decimal position. The decay rate of the wave packet $\mathcal{W}_1^6$ obtained with the few level model is two orders of magnitude smaller than the actual value in (a), while for the wave packets $\mathcal{W}_2^6$ and $\mathcal{W}_3^6$ the orders of magnitude in (a) and (b) are the same. This result implies that there are resonances with non-negligible overlap with the wave packets which have a significant contribution to the decay rates and have not been included in the model.

Figure 13 (left) shows the overlaps between the wave packets and the elements in the basis. By analyzing these overlaps it is easy to identify the specific couplings that produce the nondispersive wave packets that are summarized in Fig. 13 (right): the wave packet $\mathcal{W}_1^6$ is produced by a direct coupling between the states $^3S\mathcal{F}_1^6$ and $^3P\mathcal{G}_1^6$; the wave packet $\mathcal{W}_2^6$ is also produced by a direct coupling, but in this case between the frozen planet states $^3S\mathcal{F}_2^6$ and $^3P\mathcal{F}_1^6$; and, finally, the wave packet $\mathcal{W}_3^6$ is produced by an indirect coupling between the states $^3S\mathcal{F}_3^6$ and $^3P\mathcal{G}_1^6$.

In Table V, the wave packet $\mathcal{W}_3^6$ features the lowest decay rate. This might be related to the fact that the wave packet $\mathcal{W}_3^6$ is produced by an indirect coupling. In this sense, this long-life wave packet might be a consequence of the interplay of different decay channels with associated partial decay rates. However, the complex rotation method only provides information about the total decay rate. Another possible cause of this small decay rate might be the extension of the associated regular island in the transverse direction. In any case, this requires further investigation.

TABLE V. Energies and decay rates of the triplet wave packets $\mathcal{W}_m^6$ obtained after diagonalization of Eq. (31) for driving field parameters $F = 5.5 \times 10^{-6}$ a.u. and $\omega = 0.0012$ a.u. (a) Results using the atomic basis which includes the states of Fig. 7 with $k_{\min} = -7$ and $k_{\max} = 7$. (b) Values obtained with the few level model for $k_{\min} = -1$ and $k_{\max} = 2$.

	(a)		(b)	
m	$-E$ (a.u.)	$\Gamma/2$ (a.u.)	$-E$ (a.u.)	$\Gamma/2$ (a.u.)
1	0.073 149 52	0.000 001 24	0.073 165 98	0.000 000 03
2	0.071 743 79	0.000 002 56	0.071 748 71	0.000 001 87
3	0.070 766 20	0.000 000 58	0.070 772 79	0.000 000 38

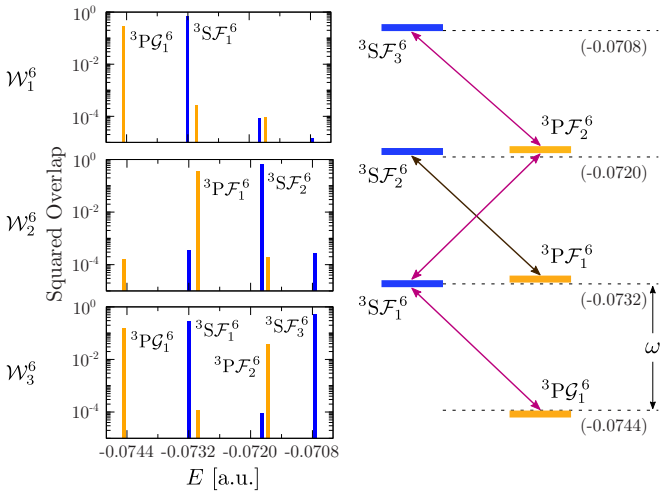

FIG. 13. Left plots display the overlaps between the wave packets obtained with the few level model and the atomic states in Table IV. In the right plot, we present the scheme of the essential states involved in the formation of the NDWP $\mathcal{W}_2^6$, $\mathcal{W}_3^6$, and $\mathcal{W}_4^6$. The dashed lines are separated by ω, with energies (in atomic units) indicated in parentheses. ^3S (^3P) states are highlighted in blue (orange).

All the atomic states in the model are frozen planet states except the state we have denoted by $^3P\mathcal{G}_1^6$. However, this state corresponds to the ground state of a series of FPS-like states that share most of the properties with the FPS (as we observe in Fig. 14), but with lower expectation value of $\cos(\theta_{12})$. For instance, the value of $\langle\cos(\theta_{12})\rangle$ for the state $^3P\mathcal{F}_1^6$ is 0.836, while for the state $^3P\mathcal{G}_1^6$ it is 0.592.

"Hyperbolic" and "elliptic" NDWPs

By looking at the Husimi distributions in Fig. 8, a question arises: why is the wave packet $\mathcal{W}_2^6$ anchored to the hyperbolic fixed point of the resonance, whereas the wave packet $\mathcal{W}_3^6$ is anchored to the elliptic fixed point of the resonance?

As we can see in Fig. 13, the wave packet $\mathcal{W}_2^6$ is produced by the coupling between the states $^3S\mathcal{F}_2^6$ and $^3P\mathcal{F}_1^6$, and its largest overlap is with the state $^3S\mathcal{F}_2^6$. However, there is a second Floquet eigenstate which is also produced by the

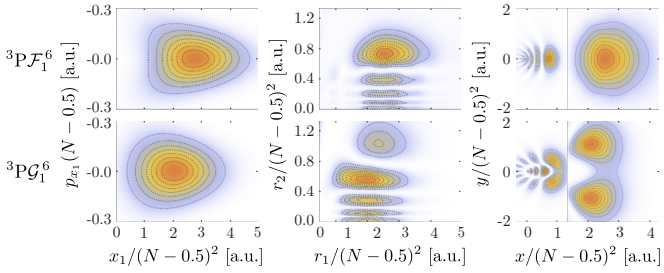

FIG. 14. Comparison between the unperturbed states $^3P\mathcal{F}_1^6$ and $^3P\mathcal{G}_1^6$. The left plots show the projections of the electronic density in phase space, while the projections of the electronic density in configuration space are depicted as a function of the distances r_1 and r_2 (for $\theta_{12} = 0$) in the center plots, and for the x and y coordinates (as in Fig. 3) in the right plots.

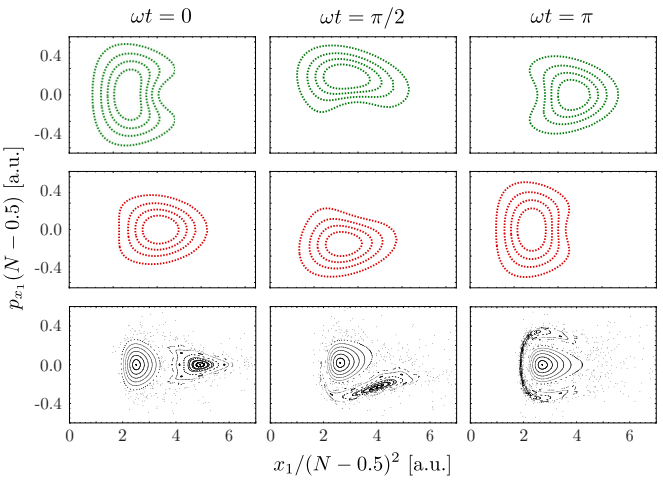

FIG. 15. Husimi distributions of the "hyperbolic" (green) and "elliptic" (red) wave packets $\mathcal{W}_2^6$ for electromagnetic driving at frequency $\omega = 0.0012$ a.u. and amplitude $F = 5.5 \times 10^{-6}$ a.u., depicted for different phases of the driving field.

coupling between the same two atomic states, but with the largest overlap with the state ${}^3P\mathcal{F}_2^6$. The latter corresponds to a wave packet anchored to the elliptic fixed point of the resonance while the former is anchored to the hyperbolic fixed point (see Fig. 15).

Figure 16 shows the energy of the two wave packets $\mathcal{W}_2^6$ (top) and the overlaps of the hyperbolic wave packet $\mathcal{W}_2^6$ with the elements in the basis (bottom), as a function of the field parameters. In the left plots, the energy and overlaps are depicted against the field amplitude F for fixed frequency $\omega = 0.0012$ a.u. For field amplitudes $F > 2 \times 10^{-6}$ a.u. (for which the contribution of the states ${}^3S\mathcal{F}_2^6$ and ${}^3P\mathcal{F}_1^6$ to the wave packet $\mathcal{W}_2^6$ remains nearly constant) the wave-packet energies exhibit slopes of similar magnitude with opposite sign. In the right plot, where the energy and overlaps are given as a function of the frequency ω for fixed field amplitude $F = 5.5 \times 10^{-6}$ a.u., we observe that, for driving frequency $\omega < 0.00124$ a.u.

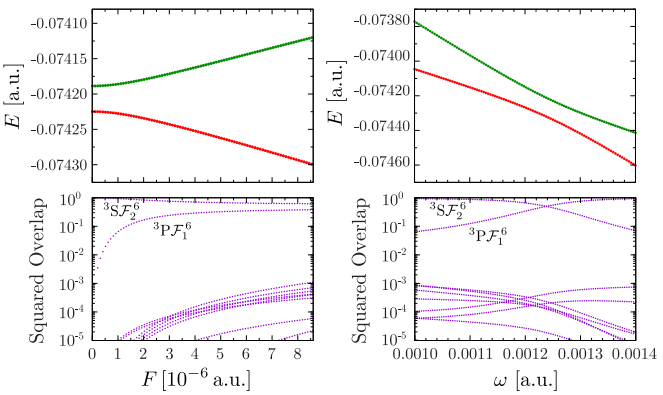

FIG. 16. Energy of the "hyperbolic" (green) and "elliptic" (red) wave packets $\mathcal{W}_2^6$ obtained with the few level model (top). Overlaps between the hyperbolic wave packet $\mathcal{W}_2^6$ and the elements in the atomic basis (bottom). The results are presented for variable field amplitude with fixed frequency $\omega = 0.0012$ a.u. (left) and variable field frequency with fixed amplitude $F = 5.5 \times 10^{-6}$ a.u. (right).

TABLE VI. Driving field parameters and converged values for the energies and decay rates of the wave packets $\mathcal{W}_2^N$.

N	ω (a.u.)	F (a.u.)	$-E$ (a.u.)	$\Gamma/2$ (a.u.)
		Singlet states		
3	0.006 60	2.0×10^{-5}	0.329 338 5	0.000 000 5
4	0.003 60	1.0×10^{-5}	0.175 724 3	0.000 002 2
5	0.002 40	2.0×10^{-5}	0.106 898 2	0.000 004 2
6	0.001 25	1.5×10^{-6}	0.071 813 9	0.000 003 9
7	0.000 80	2.0×10^{-6}	0.051 580	0.000 002
		Triplet states		
3	0.008 50	5.0×10^{-5}	0.341 003	0.000 001
4	0.004 10	4.0×10^{-5}	0.175 471 2	0.000 002 6
5	0.002 10	1.2×10^{-5}	0.106 866 5	0.000 001 4
6	0.001 24	1.5×10^{-6}	0.071 801 4	0.000 000 9
7	0.000 80	2.0×10^{-6}	0.051 575 5	0.000 000 6

(before the avoided crossing), the hyperbolic wave packet $\mathcal{W}_2^6$ has the largest overlap with the state ${}^3S\mathcal{F}_2^6$, while, for frequency $\omega > 0.00124$ a.u. (after the avoided crossing), the largest overlap is with the state ${}^3P\mathcal{F}_2^6$. The opposite is true for the elliptic wave packet.

The previous results suggest that the coupling between a FPS of $L = 0$ and a FPS of $L = 1$ produces two NDWPs, one of them anchored to the hyperbolic fixed point of the resonance and the other one anchored to the elliptic fixed point of the resonance. Which one of the coupled states has the largest overlap with the wave packet depends on the driving field parameters as we observe in Fig. 16.

D. Identification of NDWPs below other ionization thresholds

In this section, we study the dynamics of the driven frozen planet states below the $N = 3, \ldots, 7$ ionization thresholds. Based on the results of the previous section, here we look for elliptic wave packets $\mathcal{W}_2^N$ produced by the direct coupling between the frozen planet states $S\mathcal{F}_2^N$ and $P\mathcal{F}_1^N$. In each case, we construct the atomic basis (30) including only the resonances converging to the ionization threshold of interest for $L = 1, \ldots, 5$ and 11 Floquet blocks ($k_{\min} = -5$ and $k_{\max} = 5$). In this basis we solve the eigenvalue problem (31) for driving field frequency $\omega \approx |E(S\mathcal{F}_2^N) - E(P\mathcal{F}_1^N)|$ and field amplitude $F < F_I$.

In Table VI we present the field parameters used in each calculation and the converged values for the energy and decay rates of the elliptic wave packets $\mathcal{W}_2^N$ identified in the Floquet spectrum. As we described in Sec. VII B, there is an interval for the field amplitude F and frequency ω where the wave packet exhibits the nondispersive behavior. Thus, the values in Table VI should be taken as reference values, since by changing the field parameters the wave-packet energy and decay rate can also change.

Figure 17 shows the Husimi distributions of the triplet wave packets for three different phases of the driving field. The Husimi distributions for the singlet wave packets are qualitatively similar and are not presented. The wave packets are more localized by increasing N. The same behavior was observed for the NDWP in one-dimensional helium [42].

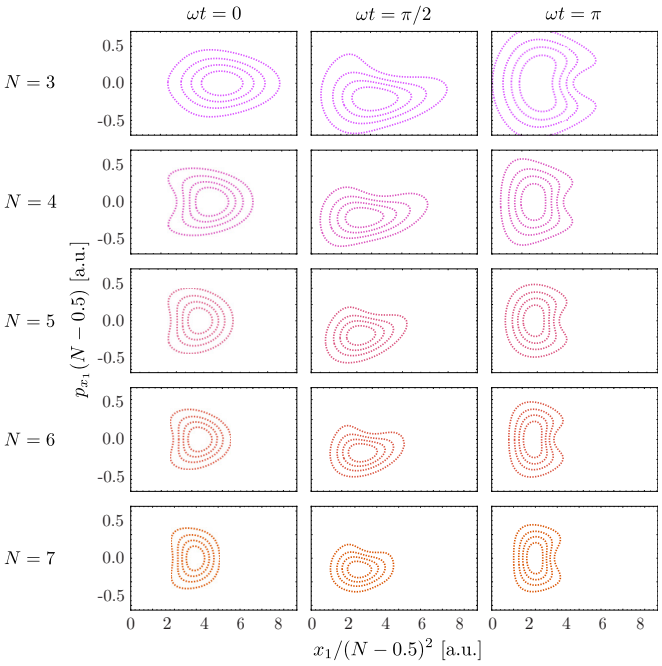

FIG. 17. Contour plot of the Husimi distribution of the triplet elliptic wave packets $\mathcal{W}_2^N$, obtained by diagonalization of Eq. (31) for the field parameters in Table VI, at different phases of the driving field.

VIII. SUMMARY AND CONCLUSIONS

We have given a full characterization of two-electron nondispersive wave packets in planar helium. Our numerical treatment, which combines a spectral method with Floquet theory, provides an efficient description of the dynamics of driven doubly excited states of planar helium with a low computational cost. The results obtained showed that the main contribution to the wave packets is given by a small number of atomic states of low angular momentum. Indeed, we have been able to reduce the system to its very basic ingredients, finding that the coupling between two frozen planet states of different angular momentum produces a "hyperbolic" and an "elliptic" nondispersive wave packet.

The method developed can be adapted to investigate the dynamics of driven frozen planet states in the full three-dimensional helium atom. In that case, we also expect that the coupling between two FPSs of different angular momentum could produce nondispersive wave packets following the classical trajectory as in the planar system. The main difference is expected to be found in the wave-packet lifetime since this value depends on the lifetime of the FPS. Though the planar model allows for quantitatively reliable predictions, the lifetimes of planar FPSs might differ from the exact ones [46].

ACKNOWLEDGMENTS

A.G. gratefully acknowledges support from COLCIENCIAS (Scholarship Program No. 6172) and Contract No. 71003. J.M. acknowledges support from the Colombian Science, Technology, and Innovation Fund-General Royalties System (Fondo CTeI-SGR) Contract No. BPIN 2013000100007. We acknowledge support from the Universidad del Valle (Proyecto de convocatoria interna CI 71102).

[1] M. Ossiander, F. Siegrist, V. Shirvanyan, R. Pazourek, A. Sommer, T. Latka, A. Guggenmos, S. Nagele, J. Feist, J. Burgdörfer *et al.*, Nat. Phys. **13**, 280 (2017).
[2] D. Busto, L. Barreau, M. Isinger, M. Turconi, C. Alexandridi, A. Harth, S. Zhong, R. J. Squibb, D. Kroon, S. Plogmaker *et al.*, J. Phys. B **51**, 044002 (2018).
[3] S. Beaulieu, A. Comby, A. Clergerie, J. Caillat, D. Descamps, N. Dudovich, B. Fabre, R. Géneaux, F. Légaré, S. Petit *et al.*, Science **358**, 1288 (2017).
[4] M. Nisoli, P. D. F. Calegari, A. Palacios, and F. Martín, Chem. Rev. **117**, 10760 (2017).
[5] M. Klinker, C. Marante, L. Argenti, J. González-Vázquez, and F. Martín, Chem. Phys. Lett. **9**, 756 (2018).
[6] A. Schiffrin, T. Paasch-Colberg, N. Karpowicz, V. Apalkov, D. Gerster, S. Mühlbrandt, M. Korbman, J. Reichert, M. Schultze, S. Holzner *et al.*, Nature (London) **493**, 70 (2013).
[7] M. T. Hassan, T. T. Luu, A. M. O. Raskazovskaya, P. Zhokhov, M. Garg, N. Karpowicz, A. M. Zheltikov, V. Pervak, F. Krausz, and E. Goulielmakis, Nature (London) **530**, 66 (2016).
[8] M. Schultze, Laser Sci. LW5F.1 (2017), doi: 10.1364/LS.2017.LW5F.1.
[9] G. Sansone, F. Kelkensberg, J. F. Pérez-Torres, F. Morales, M. F. Kling, W. Siu, O. Ghafur, P. Johnsson, M. Swoboda, E. Benedetti *et al.*, Nature (London) **465**, 763 (2010).
[10] A. S. Alnaser, M. Kübel, R. Siemering, B. Bergues, N. G. Kling, K. J. Betsch, Y. Deng, J. Schmidt, Z. A. Alahmed, A. M. Azzeer *et al.*, Nat. Comm. **5**, 3800 EP (2014)
[11] T. Okino, Y. Furukawa, Y. Nabekawa, S. Miyabe, A. Amani Eilanlou, E. J. Takahashi, K. Yamanouchi, and K. Midorikawa, Sci. Adv. **1**, e1500356 (2015).
[12] K. Hütten, M. Mittermair, S. O. Stock, R. Beerwerth, V. Shirvanyan, J. Riemensberger, A. Duensing, R. Heider, M. S. Wagner, A. Guggenmos *et al.*, Nat. Comm. **9**, 719 (2018).
[13] C. Ott, A. Kaldun, L. A., P. Raith, K. Meyer, M. Laux, Y. Zhang, A. Blättermann, S. Hagstotz, T. Ding *et al.*, Nature (London) **516**, 374 (2014).
[14] B. Bergues, M. Kübel, N. G. Johnson, B. Fischer, N. Camus, K. J. Betsch, O. Herrwerth, A. Senftleben, A. M. Sayler, T. Rathje *et al.*, Nat. Comm. **3**, 813 EP (2012)
[15] V. Gruson, L. Barreau, Á. Jiménez-Galan, F. Risoud, J. Caillat, A. Maquet, B. Carré, F. Lepetit, J.-F. Hergott, T. Ruchon *et al.*, Science **354**, 734 (2016).
[16] A. Kaldun, A. Blättermann, V. Stooß, S. Donsa, H. Wei, R. Pazourek, S. Nagele, C. Ott, C. D. Lin, J. Burgdörfer *et al.*, Science **354**, 738 (2016).
[17] F. B. Dunning, J. J. Mestayer, C. O. Reinhold, S. Yoshida, and J. Burgdörfer, J. Phys. B **42**, 022001 (2009).
[18] A. Einstein, Verhandl. Dtsc. Phys. Ges. **19**, 82 (1917).

[19] K. Richter and D. Wintgen, J. Phys. B **26**, 3719 (1993).
[20] G. Tanner, K. Richter, and J. M. Rost, Rev. Mod. Phys. **72**, 497 (2000).
[21] N. Bohr, Phil. Mag. **26**, 1 (1913).
[22] N. Bohr, Phil. Mag. **26**, 476 (1913).
[23] M. C. Gutzwiller, J. Math. Phys. **8**, 1979 (1967).
[24] M. C. Gutzwiller, J. Math. Phys. **12**, 343 (1971).
[25] J. G. Leopold and I. C. Percival, J. Phys. B **13**, 1037 (1980).
[26] G. S. Ezra, K. Richter, G. Tanner, and D. Wintgen, J. Phys. B **24**, L413 (1991).
[27] D. Wintgen, K. Richter, and G. Tanner, Chaos **2**, 19 (1992).
[28] T. Grosges, B. Piraux, and H. Bachau, Phys. Rev. A **60**, 1371 (1999).
[29] B. Piraux, J. Bauer, S. Laulan, and H. Bachau, Eur. Phys. J. D **26**, 7 (2003).
[30] L. Argenti and R. Moccia, J. Phys. B **40**, 3655 (2007).
[31] J. Eiglsperger, B. Piraux, and J. Madroñero, Phys. Rev. A **80**, 022511 (2009).
[32] L. Malegat, H. Bachau, A. Hamido, and B. Piraux, J. Phys. B **43**, 245601 (2010).
[33] R. P. Madden and K. Codling, Phys. Rev. Lett. **10**, 516 (1963).
[34] C. W. Byun, N. N. Choi, M. H. Lee, and G. Tanner, Phys. Rev. Lett. **98**, 113001 (2007).
[35] M.-H. Lee, C. W. Byun, N. N. Choi, and G. Tanner, J. Phys. B **51**, 185001 (2018).
[36] J. Eiglsperger and J. Madroñero, Phys. Rev. A **80**, 022512 (2009).
[37] T. Ericson, Phys. Rev. Lett. **5**, 430 (1960).
[38] J. Madroñero and A. Buchleitner, Phys. Rev. Lett. **95**, 263601 (2005).
[39] K. Richter and D. Wintgen, Phys. Rev. Lett. **65**, 1965 (1990).
[40] K. Richter, J. S. Briggs, D. Wintgen, and E. A. Solovev, J. Phys. B **25**, 3929 (1992).
[41] P. Schlagheck and A. Buchleitner, Europhys. Lett. **46**, 24 (1999).
[42] P. Schlagheck and A. Buchleitner, Eur. Phys. J. D **22**, 401 (2003).
[43] J. Madroñero, Ph.D. dissertation, Ludwig-Maximilians-Universität München, 2004.
[44] J. Madroñero and A. Buchleitner, Phys. Rev. A **77**, 053402 (2008).
[45] A. Buchleitner, D. Delande, and J. Zakrzewski, Phys. Rep. **368**, 409 (2002).
[46] J. Madroñero, P. Schlagheck, L. Hilico, B. Grémaud, D. Delande, and A. Buchleitner, Europhys. Lett. **70**, 183 (2005).
[47] J. Eiglsperger and J. Madroñero, Phys. Rev. A **82**, 033422 (2010).
[48] M. G. Floquet, Annales de l'École Normale Supérieure **12**, 47 (1883).
[49] J. H. Shirley, Phys. Rev. **138**, B979 (1965).
[50] B. H. Bransden, C. Joachain, and T. J. Plivier, *Physics of Atoms and Molecules* (Pearson, India, 2003).
[51] J. Aguilar and J. M. Combes, Comm. Math. Phys. **22**, 269 (1971).
[52] E. Balslev and J. M. Combes, Comm. Math. Phys. **22**, 280 (1971).
[53] B. Simon, Ann. Math. **97**, 247 (1973).
[54] W. P. Reinhardt, Annu. Rev. Phys. Chem. **33**, 223 (1982).
[55] Y. Ho, Phys. Rep. **99**, 1 (1983).
[56] S. Graffi, V. Grecchi, and H. J. Silverstone, Ann. Inst. Henri Poincaré, Phys. Théor. **42**, 215 (1985).
[57] L. Hilico, B. Grémaud, T. Jonckheere, N. Billy, and D. Delande, Phys. Rev. A **66**, 022101 (2002).
[58] R. Loudon, *The Quantum Theory of Light* (Clarendon, Oxford, 1984).
[59] D. Delande, Atomes de Rydberg en champ statiques intenses, Ph.D. thesis, Université Pierre et Marie Curie (Paris 6), 1988.
[60] D. Delande and J. Zakrzewski, Phys. Rev. A **58**, 466 (1998).
[61] J. Madroñero, A. Ponomarev, A. R. R. Carvalho, S. Wimberger, C. Viviescas, A. Kolovsky, K. Hornberger, P. Schlagheck, A. Krug, and A. Buchleitner, Adv. At. Mol. Opt. Phys. **53**, 33 (2006).
[62] C. Lanczos, J. Res. Natl. Bur. Stand. **45**, 255 (1950).
[63] A. Krug, Ph.D. dissertation, Ludwig-Maximilians-Universität München, 2001.
[64] P. Schlagheck, Ph.D. thesis, Technische Universität München, 1999.
[65] P. Kustaanheimo and E. Stiefel, J. Math. Bd **218**, 27 (1965).
[66] S. J. Aarseth and K. Zare, Celest. Mech. **10**, 185 (1974).
[67] A. J. Lichtenberg and M. A. Lieberman, *Regular and Stochastic Motion* (Springer, New York, 1983).
[68] V. N. Ostrovsky and N. V. Prudov, J. Phys. B **28**, 4435 (1995).
[69] U. Eichmann, V. Lange, and W. Sandner, Phys. Rev. Lett. **64**, 274 (1990).
[70] K. D. Heber, M. Seng, M. Halka, U. Eichmann, and W. Sandner, Phys. Rev. A **56**, 1255 (1997).
[71] P. Camus, T. F. Gallagher, J. M. Lecomte, P. Pillet, L. Pruvost, and J. Boulmer, Phys. Rev. Lett. **62**, 2365 (1989).
[72] A. Buchleitner, B. Grémaud, and D. Delande, J. Phys. B **27**, 2663 (1994).
[73] H. Friedrich and J. Trost, Phys. Rep. **397**, 359 (2004).
[74] H. Friedrich, *Theoretical Atomic Physics* (Springer, New York, 2006).
[75] R. P. Feynman, Phys. Rev. **56**, 340 (1939).
[76] H. Hellmann, *Hans Hellmann: Einführung in Die Quantenchemie: Mit Biografischen Notizen von Hans Hellmann* (Springer, New York, 2015).
[77] From the rotational invariance of the helium atom, the probability distributions depend only on the relative position of the electrons. Thus, for a given angle θ_{12} it is always possible to choose r_1 to be the Cartesian coordinate x_1, what automatically determines r_2. In particular, for $\theta_{12} = 0$ the conditional probability is obtained from the general electronic density (37) by substituting $r1 = x1$ and $r2 = x2$, with $x_1 \geqslant 0$, $x_2 \geqslant 0$, and $y_1 = y_2 = 0$.
[78] According to the Hellmann-Feynman theorem [75,76], the slope is proportional to the expectation value of the electronic dipole $\langle x_1 + x_2 \rangle$.
[79] In the few level model the atomic basis (30) includes only the unperturbed states in Table IV.